THE JOURNAL OF PHYSICAL CHEMISTRY Letters

pubs.acs.org/JPCL Letter

Stimulated X-ray Resonant Raman Spectroscopy of Conical Intersections in Thiophenol

Daeheum Cho,* Jérémy R. Rouxel, and Shaul Mukamel*

Cite This: J. Phys. Chem. Lett. 2020, 11, 4292–4297 Read Online

ABSTRACT: The conical intersection dynamics of thiophenol is studied by computing the stimulated X-ray resonant Raman spectroscopy signals. The hybrid probing field is constructed of a hard X-ray narrowband femtosecond pulse combined with an attosecond broadband X-ray pulse to provide optimal spectral and temporal resolutions for electronic coherences in the level crossing region. The signal carries phase information about the valence−core electronic coupling in the vicinity of conical intersections. Two conical intersections occurring during the course of the S−H dissociation dynamics can be distinguished by their valence−core transition frequencies computed at the complete active space self-consistent field level. The X-ray pulse is tuned such that the Raman transition at the first conical intersection between $^1\pi\sigma^*$ and $1^1\pi\pi^*$ involves higher core levels, while the Raman transition at the second conical intersection between $^1\pi\sigma^*$ and S_0 involves the lowest core level in the sulfur K-edge.

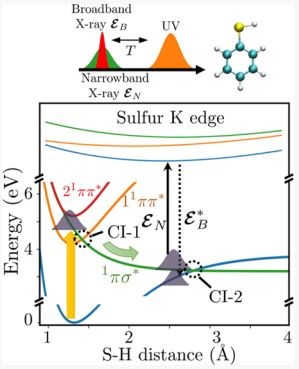

Conical intersection dynamics are essential in many photochemical reactions.[1] Nonadiabatic effects become prominent at conical intersections (CIs), where two or more electronic surfaces become energetically degenerate and the electronic and nuclear degrees of freedom are strongly coupled. Due to the strong electron−nuclear coupling at the crossing region, CIs provide an effective ultrafast nonradiative electronic decay channel for excited molecules. They play a key role in many chemical and biophysical processes, such as internal conversion, charge transfer, photoisomerization, and photodissociation.[2−8]

Probing and characterizing CIs are essential for understanding and controlling photochemical reactions. Several techniques for probing conical intersections have been proposed. These include monitoring state population dynamics,[9,10] transient vibrational/visible spectra,[11−14] and photoionization spectra.[15] Despite the many attempts, the direct unambiguous experimental observation of CI in molecules is still an open challenge. Spectroscopic techniques that probe an intrinsic property of CI, such as electronic coherence and the vanishing transition energy, are in demand.

Earlier we had proposed an off-resonant stimulated Raman technique [transient redistribution of ultrafast electronic coherences in attosecond Raman signals (TRUECARS)] for probing conical intersections in real time by monitoring electronic coherences.[16−18] In this paper, we extend this technique to the core resonant regime, thereby providing chromophore element-specific information. A hybrid X-ray probe field composed of a femtosecond narrowband (probe) and an attosecond broadband (stimulated emission) pulse provides a phase-sensitive detection of the electronic resonant Raman transition at the CI via a core excited state. X-ray pulses offer a temporal resolution that is higher than those of optical pulses due to their shorter pulse duration. We can exploit the characteristic valence−core coupling pattern of each X-ray chromophore (such as the sulfur K- and L-edges) to extract valuable insights regarding electronic excitations.

We apply this technique to probe the CI dynamics in a photodissociation of the S−H bond in thiophenol. This reaction induced by an ∼5 eV ultraviolet photon has been extensively studied.[3,19−22] Two conical intersections, CI-1 ($^1\pi\sigma^*$−$1^1\pi\pi^*$ crossing) and CI-2 ($^1\pi\sigma^*$−S_0 crossing), provide effective relaxation channels as shown in Figure 1c. Electronic coherences created at the CIs are probed in real time by the TRUECARS signal resonant with the sulfur K-edge.

TRUECARS (transient redistribution of ultrafast electronic coherences in attosecond Raman signals) Signal. Figure 1 shows (a) the setup, (b) the corresponding loop diagram, and (c) the energy level scheme. A preparation process at $T = 0$ (gray box) prepares the $|n\rangle\langle n|$ excited state, launching the nonadiabatic dynamics (see Figure 1c for the electronic states). An electronic coherence is created as the excited system approaches the CI but not by the initial preparation [$\rho_{nm}(T = 0) = 0$]. A hybrid probe pulse composed of a narrowband femtosecond pulse $\mathcal{E}_N(\omega)$ and a broadband attosecond pulse

Received: March 26, 2020
Accepted: May 5, 2020
Published: May 5, 2020

https://dx.doi.org/10.1021/acs.jpclett.0c00949
J. Phys. Chem. Lett. 2020, 11, 4292−4297

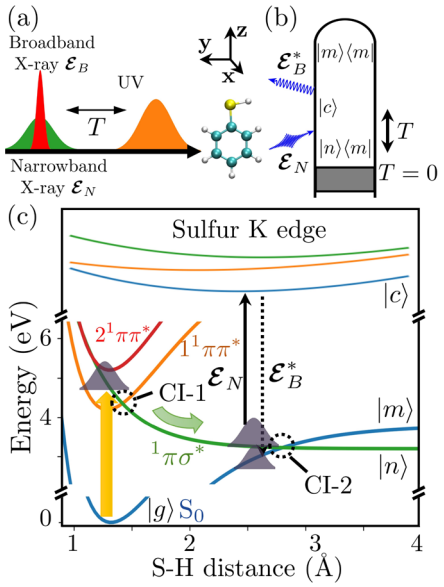

Figure 1. (a) Pulse configuration for TRUECARS, (b) loop diagram, and (c) energy level diagram on a schematic potential energy surface. A narrowband femtosecond X-ray pulse $\mathcal{E}_N$ excites an excited system on a valence electronic surface $|n\rangle$ into a core level $|c\rangle$ (sulfur K-edge) after time delay T following the arbitrary preparation (gray box) of an initial nonstationary electronic population state at $T = 0$. The signal field emission is stimulated by a broadband attosecond X-ray pulse $\mathcal{E}_B$. $^1\pi\sigma^*$, $1^1\pi\pi^*$, and $2^1\pi\pi^*$ denote the diabatic electronic basis. S_0 denotes the adiabatic ground electronic state, and S_1 and S_2 are the two lowest adiabatic excited electronic states. $|n\rangle$ ($|m\rangle$) $\in \{|S_0\rangle, ..., |S_3\rangle\}$ denotes an adiabatic valence electronic state, and $|c\rangle \in \{|c_0\rangle, ..., |c_9\rangle\}$ a sulfur K-edge state.

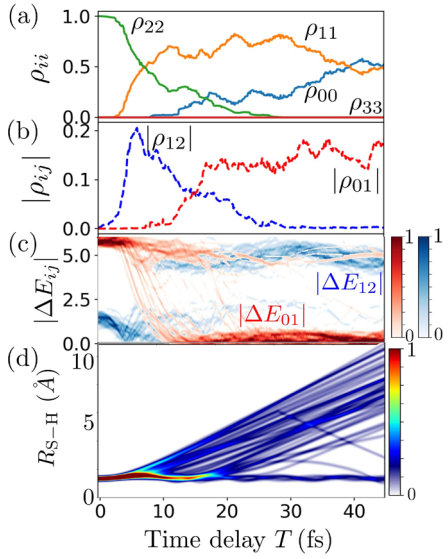

Figure 2. (a) Adiabatic populations ρ_{nn} and (b) coherence $|\rho_{nm}|$. The population ρ_{nn} and the coherence $|\rho_{nm}|$ shown in panels a and b were averaged over all trajectories. Subscript $n(m)$ denotes an adiabatic state $S_{n(m)}$. (c) Energy difference between the two valence states S_n, and S_m $|\Delta E_{nm}| = |E_m - E_n|$ in electronvolts (red, $|\Delta E_{01}|$; blue, $|\Delta E_{12}|$), where E_n is the electronic energy of adiabatic state S_n. (d) S−H bond distance R_{S-H} vs time delay T. In panels c and d, color bars represent the normalized trajectory densities.

$\mathcal{E}_B(t)$ and then excitation induces a stimulated Raman process at time delay T. $\mathcal{E}_N$ causes a valence-to-core ($|n\rangle \rightarrow |c\rangle$) with a high frequency resolution. A high temporal resolution is achieved by the broadband probe (narrow in time) that stimulates the transition from the core level to a valence state ($|c\rangle \rightarrow |m\rangle$). Frequency dispersion of the broadband pulse $\mathcal{E}_N$ finally reveals the Raman resonances. Using the narrowband frequency as a reference, a signal at a positive (negative) detection frequency represents a Stokes (anti-Stokes) process. The narrowband probe bandwidth can select the valence−core electronic transition. We set the central frequencies of the two probe pulses to be the same ($\omega_N = \omega_B$).

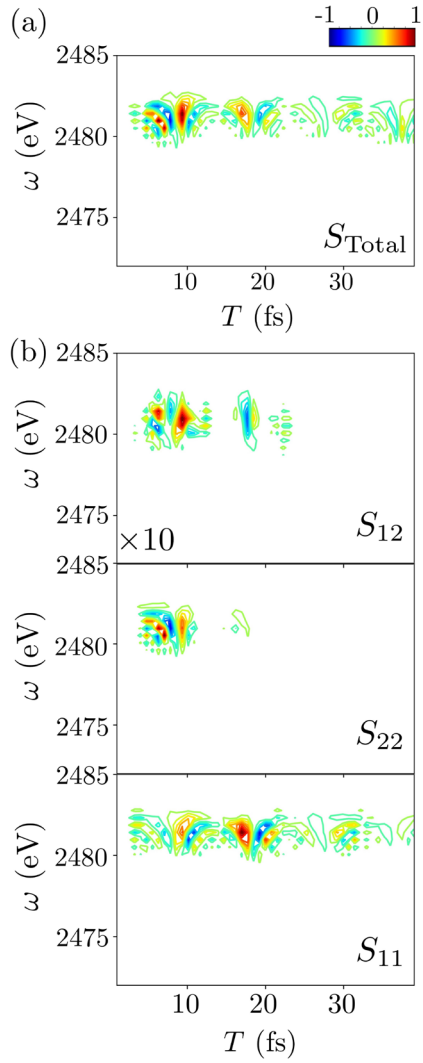

Figure 3. Simulated sulfur K-edge TRUECARS signal $S(\omega, \omega_N, T)$ (eq 3) ($\phi_N - \phi_B = 0$) for the center frequency of the narrowband probe ω_N = 2481 eV. (a) Total signal $S_{total} = \sum_{nm} S_{nm}$ where S_{nm} represents the signal contribution from the $|n\rangle\langle m|$ coherence created at the level crossing between adiabatic states S_n and S_m. (b) Dominant signal contributions S_{nm} to the total signal. The full widths at half-maximum of the narrow- and broadband probes are 2 and 20 eV, respectively.

The frequency-dispersed TRUECARS signal can be read off the diagram in Figure S1

$$S(\omega, T) = \mathcal{I}\mathcal{E}_B^*(\omega)\langle\mu(\omega)\rangle = \mathcal{I}\mathcal{E}_B^*(\omega)\int_{-\infty}^{\infty} dt\langle\mu(t)\rangle e^{i\omega t} \quad (1)$$

https://dx.doi.org/10.1021/acs.jpclett.0c00949
J. Phys. Chem. Lett. 2020, 11, 4292−4297

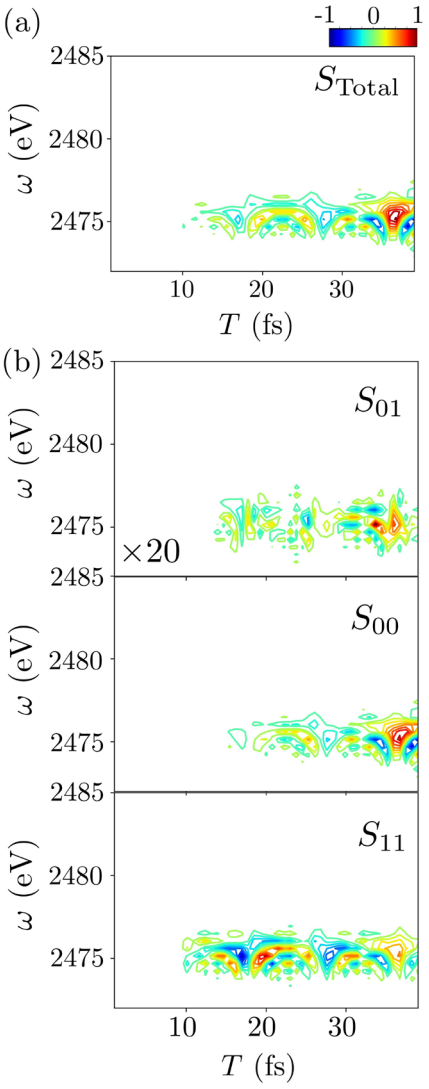

Figure 4. Same as Figure 3 but for the center frequency of the narrowband probe ω_N = 2475 eV. (b) Dominant signal contributions S_{01}, S_{00}, and S_{11} to the total signal.

$$= \mathcal{R}\mathcal{E}_B^*(\omega)\int_{-\infty}^{\infty} dt \int_0^{\infty} ds_1 \mathcal{E}_N(t - s_1 - T) \times \langle \Psi(t_0)|G^{\dagger}(t, t_0)VG(t, t - s_1)V^{\dagger}G(t - s_1, t_0)|\Psi(t_0)\rangle e^{i\omega t} \quad (2)$$

where $\langle\mu(\omega)\rangle$ and $\langle\mu(t)\rangle$ are the expectation values of the electric dipole operator in frequency and time domains, respectively. $\mathcal{E}_B$ and $\mathcal{E}_N$ are incoming broadband and narrowband probe pulses, respectively. The bold symbol $\boldsymbol{\mathcal{E}}_i$ represent the i incoming pulse and the plain symbol $\mathcal{E}_i$ its Gaussian envelope. We have used $\boldsymbol{\mathcal{E}}_i(t) = \mathcal{E}_i(t)e^{-i\omega_i t}e^{i\phi_i}$ where ω_i the center frequency of the pulse and ϕ_i the phase. $\Psi(t_0)$ is the wave function prepared at time t_0. $G^{(\dagger)}(\tau_1, \tau_2)$ is an (advanced) Green's function that propagates the electronic wave function from τ_2 to τ_1. $V^{(\dagger)}$ is an electronic annihilation (creation) operator, and s_1 is the propagation time in core state $|c\rangle$. $\mathcal{I}$ and $\mathcal{R}$ denote the imaginary and real parts of the signal, respectively. By assuming that the nuclear rearrangement during the propagation on the core excited state $|c\rangle$ is

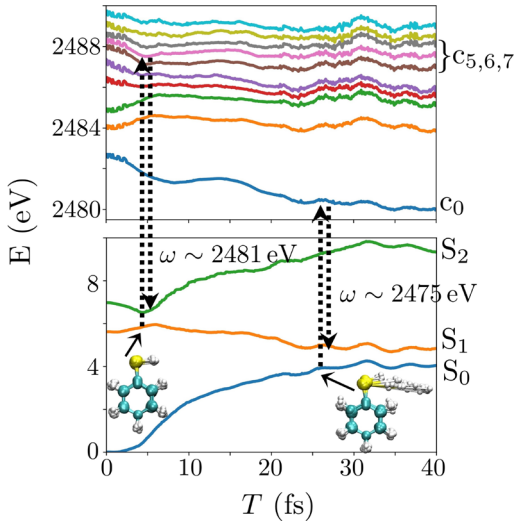

Figure 5. Adiabatic electronic energies of the valence (bottom) and core (top) levels. Geometries from all of the trajectories at 5 and 25 fs are plotted in the insets. The average S−H distances are 1.499 and 3.454 Å at 5 and 25 fs, respectively. See Figure S2 for the adiabatic electronic energies of the valence states of all trajectories.

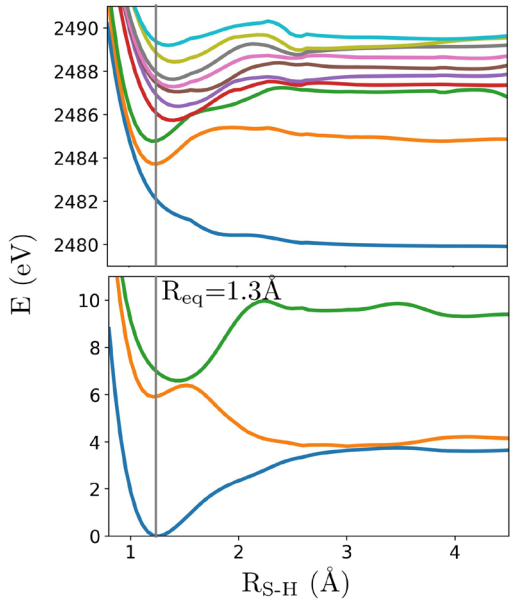

Figure 6. Adiabatic potential energy surface profiles of thiophenol in the three lowest valence and the ten lowest sulfur K-edge core levels, as a function of the S−H bond distance at the CASSCF(4/6)/6-31G* level. Ground state equilibrium S−H bond length R_{eq} = 1.3 Å (gray vertical line).

negligible (see the Supporting Information for detailed discussion and derivation), the signal becomes

$$S(\omega, \omega_N, T) = \mathcal{R}\mathcal{E}_B^*(\omega)\sum_{nmc}\int_{-\infty}^{\infty} dt \int_0^{\infty} ds_1 e^{i(\omega-\omega_N)(t-T)} \times \mathcal{E}_N(t - s_1 - T)c_n(t - s_1)c_m^*(t)\mu_{mc}(t)\mu_{cn}^{\dagger}(t - s_1) \times e^{-i(\omega_c-\omega_N)s_1}e^{i(\phi_N-\phi_B)} \quad (3)$$

where $\mathcal{E}_B(\omega)$ is a Gaussian broadband pulse envelope, $\mathcal{E}_N(t - s_1 - T)$ is a Gaussian envelope in the time domain for the narrowband probe centered at $t = T$, and ϕ_i is the phase

https://dx.doi.org/10.1021/acs.jpclett.0c00949
J. Phys. Chem. Lett. 2020, 11, 4292−4297

of the $\boldsymbol{\mathcal{E}}_i$ pulse. $c_n(t)$ is a wave function coefficient of adiabatic electronic state $\psi_n(t)$ at time t, which involves the phase of the electronic wave function. The transition dipole moment matrix elements μ_{ij} are the components along the incoming field polarizations. $\omega_c = E_c/\hbar$ is an energy of the core state $|c\rangle$ at time t, ω_N is the frequency of the narrowband probe $\boldsymbol{\mathcal{E}}_N$, and $\boldsymbol{\mu}_{nc}$ represents the transition dipole moments between valence n and core c states. Equation 3 will be used to calculate the TRUECARS signals. The wave function coefficients $c_i(t)$ in adiabatic basis are obtained from a nonadiabatic dynamics simulation. We shall factorize them as $c_n(t) = \tilde{c}_n(t)e^{-i\omega_n t}$. Equation 3 can then be recast as

$$S(\omega, \omega_N, T) = \mathcal{R}\mathcal{E}_B^*(\omega)\sum_{nmc}\int_{-\infty}^{\infty} dt \int_0^{\infty} ds_1 \; e^{i(\omega-\omega_N-\omega_{nm})(t-T)}\mathcal{E}_N(t-s_1-T)\tilde{c}_n(t-s_1)\tilde{c}_m^*(t) \; \mu_{mc}(t)\mu_{cn}^{\dagger}(t-s_1)e^{-i(\omega_{cn}-\omega_N)s_1}e^{i(\phi_N-\phi_B)} \quad (4)$$

We need to meet two resonance conditions: $\omega_N = \omega_{cn}$ and $\omega = \omega_N + \omega_{nm} = \omega_{cm}$. The first condition is the resonance between narrowband probe frequency ω_N and a core−valence transition frequency ω_{cn}. The second states that the signal field frequency ω is shifted by the energy gap between the two electronic surfaces ω_{nm} compared to the narrowband probe frequency ω_N.

The signal is linear in the probe field amplitude $\boldsymbol{\mathcal{E}}_B\boldsymbol{\mathcal{E}}_N$ and carries the phase factor $e^{i(\phi_N-\phi_B)}$. Controlled phases $(\phi_N - \phi_B)$ are required to generate the signal, because it vanishes upon averaging over a random phase distribution. When the two probe field phases are the same $(\phi_N = \phi_B)$, the phase of the electronic coherence can be directly measured by the signal. A phase cycling protocol[23] can be employed to extract the desired signal contribution as shown in Figure 1b, one interaction with $\boldsymbol{\mathcal{E}}_N$ and one interaction with $\boldsymbol{\mathcal{E}}_B$, out of other Raman transition processes created by two interactions with the $\boldsymbol{\mathcal{E}}_B$ or $\boldsymbol{\mathcal{E}}_N$ probe. However, the noise in the X-ray probe could be substantial; one needs to make sure that the signal does not deteriorate because of the noise of the X-ray probes.

S−H Dissociation Dynamics of Thiophenol. Numerous modeling schemes have been employed for the strongly coupled electronic and nuclear degrees of freedom in nonadiabatic photochemical reactions. These include (multiconfigurational) Ehrenfest dynamics,[24] multiconfigurational time-dependent Hartree,[25] and multiple spawning.[26] Semiclassical approaches, which treat the electrons quantum mechanically and the nuclei classically, provide a practical level of theory. Surface hopping[27,28] (SH) is the most commonly used semiclassical nonadiabatic dynamics protocol. Because the trajectories are independent of each other, special care must be made to account for nuclear coherences.

The nonadiabatic photodissociation of thiophenol was simulated using the surface hopping protocol implemented in the SHARC[29,30] program. Herein, we provide a brief summary (see the Supporting Information for computational details). The electronic structure calculations were performed using MOLPRO[31] at the state-averaged CASSCF(4/6)/6-31G* level with the four lowest adiabatic electronic basis. The local diabatization algorithm based on the overlap matrices between the adiabatic electronic states $\langle\psi_\beta(t)|\psi_\alpha(t+\Delta t)\rangle$ was used to propagate the electronic wave function under nonadiabatic couplings. We have employed the energy-based decoherence correction scheme.[32] The adiabatic electronic populations (ρ_{nn}; diagonal element of the density matrix) and the coherences (ρ_{nm}; off-diagonal element of the density matrix) in the adiabatic electronic basis were calculated from the wave function coefficient vector $\mathbf{c}(t)$, $\rho_{nn}(t) = |c_n(t)|^2$, and $\rho_{nm}(t) = c_n(t)c_m^*(t)$. The energy difference $|\Delta E_{nm}|$ is the transition energy between the two adiabatic electronic states, S_n and S_m. The valence−core transition dipole moments $\boldsymbol{\mu}_{cn}$ among the lowest three valence states and the 10 lowest core states in the S K-edge are calculated in 0.1 fs intervals along the nonadiabatic dynamics. All quantities reported in the paper are given in the adiabatic electronic basis. The overall propagation time was 49 fs, and the time steps for propagation of the nuclear and the electronic degrees of freedom were 0.05 and 0.002 fs, respectively. We sampled 45 initial geometries by using the quantum harmonic oscillator Wigner distribution around the ground state equilibrium geometry. The nonadiabatic surface hopping dynamics was initiated by preparing the system in the S_2 ($^1\pi\sigma^*$) state. The results of 45 trajectories were averaged out to provide the signals. Figures S3−S10 show the convergence of the population dynamics ρ_{nn} and coherences ρ_{12} and ρ_{01} with the number of trajectories.

We have investigated the S−H bond dissociation dynamics of thiophenol following initial excitation to S_2 ($^1\pi\sigma^*$) (the external pump pulse was not included explicitly; its inclusion in the simulation may affect the dynamics). We have previously studied this photodissociation reaction,[18] by off-resonant stimulated X-ray Raman imaging. Although diabatic state $1^1\pi\pi^*$ is bright at a long wavelength λ of >275 nm (ω < 4.5 eV), the $^1\pi\sigma^*$ excitation can be achieved at higher excitation energies.[19,20,33] The nonadiabatic dynamics following the $1^1\pi\pi^*$ excitation has been studied by several groups.[34−36]

Figure 2 shows the populations ρ_{nn}, coherences $|\rho_{nm}|$, the energy difference between two valence states S_n and S_m $|\Delta E_{nm}|$, and the S−H bond distance R_{S-H} versus time delay T. The initially excited S_2 population at $T = 0$ relaxes to ground state S_0 via the two conical intersections. As the excited system at S_2 approaches CI-1, electronic coherence between S_2 and S_1 ($|\rho_{12}|$) increases and peaks at 7 fs. The S_2 population ρ_{22} rapidly transfers to S_1 population ρ_{11} during the T = 3−13 fs interval. The energy gap between S_2 and S_1 ($|\Delta E_{12}|$) vanishes in the T = 3−8 fs interval. The existence of coherence ρ_{12} and the vanishing energy gap $|\Delta E_{12}| \sim 0$ are indicators of CI-1. Up to T = 10 fs, the S−H bond R_{S-H} does not significantly stretch as shown in Figure 2d.

As the system approaches CI-2 at T = 13 fs, the electronic coherence $|\rho_{01}|$ and thus the ground state population ρ_{00} starts to grow, while the energy gap between S_1 and S_0 ($|\Delta E_{01}|$) vanishes. A significant geometric change in the S−H distance occurs during the dynamics from CI-1 (R_{S-H} = 1.499 Å) to CI-2 (R_{S-H} = 3.454 Å). A more detailed discussion of the semiclassical dynamics can be found in ref 18.

Sulfur K-Edge TRUECARS Signal. We aim to probe the emergence of the electronic coherences at conical intersections via TRUECARS. The narrowband pulse ω_N was scanned over the sulfur K-edge regime between 2472 and 2484 eV. The signal calculated with the y-polarized probe fields is presented in Figures 3 and 4 (see Figure 1 for the coordinate system).

The TRUECARS signal shows distinct features at ω_N = 2475 and 2481 eV. As shown in Figure 3a, the signal at ω_N = 2481 eV turns on at early and fades at longer times. The total signal is dominated by S_{12}, S_{22}, and S_{11}, which represent the

https://dx.doi.org/10.1021/acs.jpclett.0c00949
J. Phys. Chem. Lett. 2020, 11, 4292−4297

$|1\rangle\langle 2|$ (coherence), $|2\rangle\langle 2|$, and $|1\rangle\langle 1|$ (population), respectively, where the total signal $S_{total} = \sum_{nm} S_{nm}$, where S_{nm} comes from $|n\rangle\langle m|$. Figure 3b shows that the population of the S_2 state (S_{22}) is transferred to S_1 and rapidly decays, while the S_1 population (S_{11}) survives longer. The signal contribution from the $|1\rangle\langle 2|$ coherence (S_{12}) comes from CI-1. We find that the S_{12} contribution is given by the stimulated resonant Raman transition between S_2 and S_1 states via c_5, c_6, and c_7 in the sulfur K-edge manifold (see Figure 6 for the energy level scheme).

The other feature at $\omega_N = 2475$ eV shown in Figure 4a turns on at 12 fs and lasts up to 40 fs. The total signal at $\omega_N = 2475$ eV is dominated by S_{01}, S_{11}, and S_{00} (populations), reflecting the signal contributed by $|0\rangle\langle 1|$ (coherence), $|1\rangle\langle 1|$, and $|0\rangle\langle 0|$ (population), respectively. The S_{01} contribution is a manifestation of the electronic coherence $|0\rangle\langle 1|$ created at CI-1. The S_{01} contribution mainly comes from the stimulated Raman transition between S_1 and S_0 states via c_0, which is the lowest state of the sulfur K-edge manifold.

The dominant Raman transitions at $\omega_N = 2475$ and 2481 eV are depicted in Figure 5 together with the valence and the core electronic energies averaged over all trajectories. (The relevant electronic electronic surfaces averaged over trajectories do not cross at the respective conical intersections because different trajectories reach the conical intersection at different times.) The two arrows at $T = 5$ fs represent the Raman transition pathway $S_1 \rightarrow c_{i\in\{5,6,7\}} \rightarrow S_2$ at CI-1, while the other at $T = 25$ fs to the pathway $S_0 \rightarrow c_0 \rightarrow S_1$ at CI-2. The difference in the electronic transition energies at $T = 5$ and 25 fs can be explained as follows. First, the electronic transition from S_2 to higher-lying core levels is stronger than to the low-lying core levels at $T = 5$ fs, while the transition from the S_0 state to the lowest core level is stronger than the higher-lying core levels at $T = 25$. Second, the lowest core level energy is stabilized in the course of the nuclear dynamics, due to S−H bond elongation. The potential energy curves in the valence and the sulfur K-edge core levels, shown in Figure 6, indeed show the significant stabilization of c_0 with S−H distance. Because of the large energy separation of peak for CI-1 at $\omega_N = 2481$ eV and CI-2 at $\omega_N = 2475$ eV and the separation in time delay T, the two conical intersections may be probed by the TRUECARS technique using the hybrid probe pulses and resolved in frequency and time.

Conclusions. We have proposed a resonant stimulated X-ray Raman TRUECARS technique to probe nonadiabatic molecular dynamics. The technique employs hybrid hard X-ray narrowband/broadband probe fields to monitor the electronic coherences at the level crossing region. The resonant stimulated Raman signal carries phase information about the valence-to-core electronic coupling in the vicinity of conical intersections. More importantly, the various conical intersections can be distinguished by the transition frequency and characteristics of the valence−core transition.

■ ASSOCIATED CONTENT

Supporting Information

The Supporting Information is available free of charge at https://pubs.acs.org/doi/10.1021/acs.jpclett.0c00949.

Derivation of the signal, additional computational details, and convergence of the population dynamics ρ_{nn} and the absolute, real, and imaginary values of two dominant coherences, ρ_{01} and ρ_{12}, according to the number of trajectories studied (PDF)

■ AUTHOR INFORMATION

Corresponding Authors

Daeheum Cho − *Department of Chemistry and Department of Physics & Astronomy, University of California, Irvine, California 92697-2025, United States;* orcid.org/0000-0002-0322-4291; Email: daeheumc@uci.edu

Shaul Mukamel − *Department of Chemistry and Department of Physics & Astronomy, University of California, Irvine, California 92697-2025, United States;* orcid.org/0000-0002-6015-3135; Email: smukamel@uci.edu

Author

Jérémy R. Rouxel − *Department of Chemistry and Department of Physics & Astronomy, University of California, Irvine, California 92697-2025, United States;* orcid.org/0000-0003-3438-6370

Complete contact information is available at: https://pubs.acs.org/10.1021/acs.jpclett.0c00949

Notes

The authors declare no competing financial interest.

■ ACKNOWLEDGMENTS

The support of the Chemical Sciences, Geosciences, and Biosciences division, Office of Basic Energy Sciences, Office of Science, U.S. Department of Energy (DOE), through Grant DE-FG02-04ER15571 and the National Science Foundation (Grant CHE-1953045) is gratefully acknowledged. D.C. was supported by the DOE grant.

■ REFERENCES

(1) Domcke, W.; Yarkony, D. R. Role of Conical Intersections in Molecular Spectroscopy and Photoinduced Chemical Dynamics. *Annu. Rev. Phys. Chem.* **2012**, *63*, 325−352.

(2) Lim, J. S.; Kim, S. K. Experimental probing of conical intersection dynamics in the photodissociation of thioanisole. *Nat. Chem.* **2010**, *2*, 627−632.

(3) You, H. S.; Han, S.; Lim, J. S.; Kim, S. K. ($\pi\pi^*/\pi\sigma^*$) Conical Intersection Seam Experimentally Observed in the S-D Bond Dissociation Reaction of Thiophenol-d_1. *J. Phys. Chem. Lett.* **2015**, *6*, 3202−3208.

(4) Musser, A. J.; Liebel, M.; Schnedermann, C.; Wende, T.; Kehoe, T. B.; Rao, A.; Kukura, P. Evidence for conical intersection dynamics mediating ultrafast singlet exciton fission. *Nat. Phys.* **2015**, *11*, 352−357.

(5) Worner, H. J.; Bertrand, J. B.; Fabre, B.; Higuet, J.; Ruf, H.; Dubrouil, A.; Patchkovskii, S.; Spanner, M.; Mairesse, Y.; Blanchet, V.; et al. Conical Intersection Dynamics in NO2 Probed by Homodyne High-Harmonic Spectroscopy. *Science* **2011**, *334*, 208−212.

(6) Horio, T.; Fuji, T.; Suzuki, Y.-I.; Suzuki, T. Probing Ultrafast Internal Conversion through Conical Intersection via Time-Energy Map of Photoelectron Angular Anisotropy. *J. Am. Chem. Soc.* **2009**, *131*, 10392−10393.

(7) Hoffman, D. P.; Ellis, S. R.; Mathies, R. A. Characterization of a Conical Intersection in a Charge-Transfer Dimer with Two-Dimensional Time-Resolved Stimulated Raman Spectroscopy. *J. Phys. Chem. A* **2014**, *118*, 4955−4965.

(8) Hoffman, D. P.; Mathies, R. A. Femtosecond Stimulated Raman Exposes the Role of Vibrational Coherence in Condensed-Phase Photoreactivity. *Acc. Chem. Res.* **2016**, *49*, 616−625.

(9) Polli, D.; Altoè, P.; Weingart, O.; Spillane, K. M.; Manzoni, C.; Brida, D.; Tomasello, G.; Orlandi, G.; Kukura, P.; Mathies, R. A.;

et al. Conical intersection dynamics of the primary photoisomerization event in vision. *Nature* **2010**, *467*, 440−443.
(10) McFarland, B. K.; Farrell, J. P.; Miyabe, S.; Tarantelli, F.; Aguilar, A.; Berrah, N.; Bostedt, C.; Bozek, J. D.; Bucksbaum, P. H.; Castagna, J. C.; et al. Ultrafast X-ray Auger probing of photoexcited molecular dynamics. *Nat. Commun.* **2014**, *5*, 4235.
(11) Raab, A.; Worth, G. A.; Meyer, H.-D.; Cederbaum, L. S. Molecular dynamics of pyrazine after excitation to the S2 electronic state using a realistic 24-mode model Hamiltonian. *J. Chem. Phys.* **1999**, *110*, 936−946.
(12) Oliver, T. A. A.; Lewis, N. H. C.; Fleming, G. R. Correlating the motion of electrons and nuclei with two-dimensional electronic-vibrational spectroscopy. *Proc. Natl. Acad. Sci. U. S. A.* **2014**, *111*, 10061−10066.
(13) Timmers, H.; Li, Z.; Shivaram, N.; Santra, R.; Vendrell, O.; Sandhu, A. Coherent Electron Hole Dynamics Near a Conical Intersection. *Phys. Rev. Lett.* **2014**, *113*, 113003.
(14) Kowalewski, M.; Mukamel, S. Stimulated Raman signals at conical intersections: Ab initio surface hopping simulation protocol with direct propagation of the nuclear wave function. *J. Chem. Phys.* **2015**, *143*, 044117.
(15) von Conta, A.; Tehlar, A.; Schletter, A.; Arasaki, Y.; Takatsuka, K.; Worner, H. J. Conical-intersection dynamics and ground-state chemistry probed by extreme-ultraviolet time-resolved photoelectron spectroscopy. *Nat. Commun.* **2018**, *9*, 3162.
(16) Kowalewski, M.; Fingerhut, B. P.; Dorfman, K. E.; Bennett, K.; Mukamel, S. Simulating Coherent Multidimensional Spectroscopy of Nonadibatic Molecular Processes: From the Infrared to the X-ray Regime. *Chem. Rev.* **2017**, *117*, 12165.
(17) Kowalewski, M.; Bennett, K.; Dorfman, K. E.; Mukamel, S. Catching Conical Intersections in the Act: Monitoring Transient Electronic Coherences by Attosecond Stimulated X-Ray Raman Signals. *Phys. Rev. Lett.* **2015**, *115*, 193003.
(18) Cho, D.; Mukamel, S. Stimulated X-ray Raman Imaging of Conical Intersections. *J. Phys. Chem. Lett.* **2020**, *11*, 33−39.
(19) Devine, A. L.; Nix, M. G. D.; Dixon, R. N.; Ashfold, M. N. R. Near-Ultraviolet Photodissociation of Thiophenol. *J. Phys. Chem. A* **2008**, *112*, 9563−9574.
(20) Lim, J. S.; Choi, H.; Lim, I. S.; Park, S. B.; Lee, Y. S.; Kim, S. K. Photodissociation Dynamics of Thiophenol-d_1: The Nature of Excited Electronic States along the S-D Bond Dissociation Coordinate. *J. Phys. Chem. A* **2009**, *113*, 10410−10416.
(21) Lim, I. S.; Lim, J. S.; Lee, Y. S.; Kim, S. K. Experimental and theoretical study of the photodissociation reaction of thiophenol at 243nm: Intramolecular orbital alignment of the phenylthiyl radical. *J. Chem. Phys.* **2007**, *126*, 034306.
(22) Ashfold, M. N. R.; Devine, A. L.; Dixon, R. N.; King, G. A.; Nix, M. G. D.; Oliver, T. A. A. Exploring nuclear motion through conical intersections in the UV photodissociation of phenols and thiophenol. *Proc. Natl. Acad. Sci. U. S. A.* **2008**, *105*, 12701−12706.
(23) Hamm, P.; Zanni, M. *Concepts and Methods of 2D Infrared Spectroscopy*; Cambridge University Press: Cambridge, U.K., 2011.
(24) Shalashilin, D. V. Multiconfigurational Ehrenfest approach to quantum coherent dynamics in large molecular systems. *Faraday Discuss.* **2011**, *153*, 105.
(25) Meyer, H.-D.; Worth, G. A. Quantum molecular dynamics: propagating wavepackets and density operators using the multi-configuration time-dependent Hartree method. *Theor. Chem. Acc.* **2003**, *109*, 251−267.
(26) Ben-Nun, M.; Quenneville, J.; Martínez, T. J. Ab Initio Multiple Spawning: Photochemistry from First Principles Quantum Molecular Dynamics. *J. Phys. Chem. A* **2000**, *104*, 5161−5175.
(27) Tully, J. C.; Preston, R. K. Trajectory Surface Hopping Approach to Nonadiabatic Molecular Collisions: The Reaction of H^+ with D_2. *J. Chem. Phys.* **1971**, *55*, 562−572.
(28) Subotnik, J. E.; Jain, A.; Landry, B.; Petit, A.; Ouyang, W.; Bellonzi, N. Understanding the Surface Hopping View of Electronic Transitions and Decoherence. *Annu. Rev. Phys. Chem.* **2016**, *67*, 387−417.
(29) Mai, S.; Marquetand, P.; González, L. A general method to describe intersystem crossing dynamics in trajectory surface hopping. *Int. J. Quantum Chem.* **2015**, *115*, 1215−1231.
(30) Richter, M.; Marquetand, P.; González-Vázquez, J.; Sola, I.; González, L. SHARC: ab initio Molecular Dynamics with Surface Hopping in the Adiabatic Representation Including Arbitrary Couplings. *J. Chem. Theory Comput.* **2011**, *7*, 1253−1258.
(31) Werner, H.-J.; Knowles, P. J.; Knizia, G.; Manby, F. R.; Schütz, M. Molpro: a general-purpose quantum chemistry program package. *WIREs Comput. Mol. Sci.* **2012**, *2*, 242−253.
(32) Granucci, G.; Persico, M.; Zoccante, A. Including quantum decoherence in surface hopping. *J. Chem. Phys.* **2010**, *133*, 134111.
(33) Venkatesan, T. S.; Ramesh, S. G.; Lan, Z.; Domcke, W. Theoretical analysis of photoinduced H-atom elimination in thiophenol. *J. Chem. Phys.* **2012**, *136*, 174312.
(34) Yang, K. R.; Xu, X.; Zheng, J.; Truhlar, D. G. Full-dimensional potentials and state couplings and multidimensional tunneling calculations for the photodissociation of phenol. *Chem. Sci.* **2014**, *5*, 4661−4680.
(35) Xu, X.; Zheng, J.; Yang, K. R.; Truhlar, D. G. Photodissociation Dynamics of Phenol: Multistate Trajectory Simulations including Tunneling. *J. Am. Chem. Soc.* **2014**, *136*, 16378−16386.
(36) Xie, C.; Ma, J.; Zhu, X.; Yarkony, D. R.; Xie, D.; Guo, H. Nonadiabatic Tunneling in Photodissociation of Phenol. *J. Am. Chem. Soc.* **2016**, *138*, 7828−7831.

https://dx.doi.org/10.1021/acs.jpclett.0c00949
J. Phys. Chem. Lett. 2020, 11, 4292−4297

-SUPPORTING INFORMATION-

for

Stimulated X-ray Resonant Raman Spectroscopy of Conical Intersections in Thiophenol

Daeheum Cho,* Jérémy R. Rouxel, and Shaul Mukamel*

Departments of Chemistry, University of California, Irvine, California 92697-2025, United States

E-mail: daeheumc@uci.edu; smukamel@uci.edu

Signal derivation

To compute the signal, we use a wave-function based approach that is more convenient than the density matrix based ones when the dynamics is propagated numerically. The loop diagram rules have been given in previous publications[1,2] and here we only describe the dynamics along the loop. In Figure S1, the shaded area represents a preparation step of the molecular excited state, typically involving an ultrashort laser pulse incident at time t_0. The left branch of the loop represents the time evolution of the ket until the expectation value is taken at time t and the right branch represent the time evolution of the bra. The ket evolves first with the propagator $G(t - s_1 - t_0)$ from time t_0 to time $t - s_1$. This propagator includes both the state preparation (shaded area) and the numerically propagated non-adiabatic dynamics (dashed line). The non-adiabatic dynamics populates the state n that is then probed with a delayed pulse (time delay T) through a Raman process represented by the arrows in diagram shown in Figure S1. At time $t - s_1$, a photon is absorbed and the wavepacket is sent onto state c. The core state being extremely short lived, we neglect the nuclear dynamics during time s_1 and the propagation is then represented by a solid line. At time t, the second interaction with the probe brings down the wavepacket into state m. The signal is finally obtained as a scalar product between the propagated ket and bra at time t. As shown in Figure S1, no perturbative interaction with the incoming X-ray fields is considered in the right branch and the bra is propagated from t_0 to t using the propagator $G^\dagger(t-t_0)$, which describes the nonadiabatic dynamics without external fields.

The frequency dispersed TRUECARS signal is given by

$$S_{\mathrm{ram}}(\omega) = \Im \boldsymbol{\mathcal{E}}_B^*(\omega) \cdot \langle \boldsymbol{\mu}(\omega) \rangle \tag{S1}$$

with

$$\langle \boldsymbol{\mu}(\omega) \rangle = \int dt e^{i\omega t} \langle \boldsymbol{\mu}(t) \rangle \tag{S2}$$

where $\langle\mu(\omega)\rangle$ and $\langle\mu(t)\rangle$ are the expectation value of the electric dipole operator in frequency and time domains, respectively. $\boldsymbol{\mathcal{E}}_B$ is the incoming broadband probe pulse. $\Im$ and $\Re$ denote the imaginary and real parts of the signal, respectively.

We now expand perturbatively following the loop diagram in Figure S1 and obtain:

$$\langle\boldsymbol{\mu}(t)\rangle = -i\int ds_1\langle\Psi(t_0)|G^\dagger(t,t_0)VG(t,t-s_1)V^\dagger G(t-s_1,t_0)|\Psi(t_0)\rangle\boldsymbol{\mathcal{E}}_N(t-s_1-T) \quad \text{(S3)}$$

where $\Psi(t_0)$ is the total wavefunction prepared at time t_0, $G^{(\dagger)}(\tau_1,\tau_2)$ is a (advanced) Green's function that propagates the electronic wavefunction from τ_2 to τ_1, $V^{(\dagger)}$ is an electron annihilation (creation) operator, and s_1 is the propagation time in a core state $|c\rangle$. $\langle\mu(\omega)\rangle$ and $\langle\mu(t)\rangle$ are the expectation value of the electric dipole operator in frequency and time domains, respectively. $\boldsymbol{\mathcal{E}}_N$ is the narrowband probe pulse.

Summing over states leads to:

$$\begin{aligned}\langle\boldsymbol{\mu}(t)\rangle = -i\sum_{nmc}\int ds_1\langle\Psi(t_0)|G^\dagger(t-t_0)|m\rangle\boldsymbol{\mu}_{mc}(t-t_0)G_c(s_1)\\ \times\boldsymbol{\mu}^\dagger_{cn}(t-s_1-t_0)\langle n|G(t-s_1-t_0)|\Psi(t_0)\rangle\boldsymbol{\mathcal{E}}_N(t-s_1-T) \quad \text{(S4)}\end{aligned}$$

where $G_c(s_1)$ describes the electronic modulation in core state $|c\rangle$ during s_1, and $\boldsymbol{\mu}_{mc}(t)$ is the transition dipole moment between valence $|m\rangle$ and core $|c\rangle$ states.

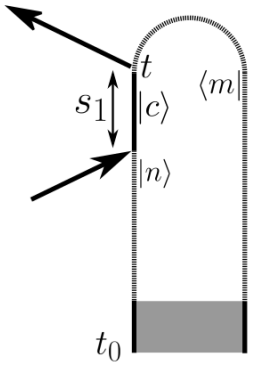

Figure S1: A loop diagram for the stimulated X-ray Raman spectroscopy.

We now set $t_0 = 0$ for simplicity and define

$$\langle \Psi(t_0)|G^\dagger(t-t_0)|m\rangle = c_m^*(t) \tag{S5}$$

$$\langle n|G(t-s_1-t_0)|\Psi(t_0)\rangle = c_n(t-s_1) \tag{S6}$$

$$G_c(s_1) = e^{-i\omega_c s_1} \tag{S7}$$

In eq. S7, we have neglected the time evolution of the geometry in the core states c during the dummy interval s_1. The wavefunction coefficients c_n in an adiabatic basis shown in eq. S5 and S6 can be obtained from the nonadiabatic simulations. The frequency of the electronic modulation in the core state $|c\rangle$, $\omega_c = E_c\hbar$, can be obtained by valence-to-core transition calculations along with the nonadiabatic dynamics. Gathering these terms together, we get

$$\langle \boldsymbol{\mu}(t)\rangle = -i\int ds_1 c_m^*(t)c_n(t-s_1)\boldsymbol{\mu}_{mc}(t)\boldsymbol{\mu}_{cn}^\dagger(t-s_1)e^{-i\omega_c s_1}\boldsymbol{\mathcal{E}}_N(t-s_1-T) \tag{S8}$$

and the signals becomes

$$\begin{aligned}
S_{\mathrm{ram}}(\omega,\omega_N,T) &= \Re\mathcal{E}_B^*(\omega)\sum_{nmc}\int_{-\infty}^{\infty}dt e^{i\omega(t-T)}\int_0^\infty ds_1\boldsymbol{\mathcal{E}}_N(t-s_1-T) \\
&\qquad \times c_n(t-s_1)c_m^*(t)\mu_{mc}(t)\mu_{cn}^\dagger(t-s_1)e^{-i\omega_c s_1}e^{i(\phi_N-\phi_B)} \\
&= \Re\mathcal{E}_B^*(\omega)\sum_{nmc}\int_{-\infty}^{\infty}dt\int_0^\infty ds_1 e^{i\omega(t-T)}\boldsymbol{\mathcal{E}}_N(t-s_1-T)c_m^*(t)\mu_{mc}(t)c_n(t-s_1)\mu_{cn}^\dagger(t-s_1)e^{-i\omega_c s_1}e^{i(\phi_N-\phi_B)} \\
&= \Re\mathcal{E}_B^*(\omega)\sum_{nmc}\int_{-\infty}^{\infty}dt\int_0^\infty ds_1 e^{i\omega(t-T)}\mathcal{E}_N(t-s_1-T)e^{-\omega_N(t-s_1-T)}c_m^*(t)\mu_{mc}(t)c_n(t-s_1)\mu_{cn}^\dagger(t-s_1) \\
&\qquad \times e^{-i\omega_c s_1}e^{i(\phi_N-\phi_B)} \\
&= \Re\mathcal{E}_B^*(\omega)\sum_{nmc}\int_{-\infty}^{\infty}dt\int_0^\infty ds_1 e^{i(\omega-\omega_N)(t-T)}\mathcal{E}_N(t-s_1-T)c_n(t-s_1)c_m^*(t)\mu_{mc}(t)\mu_{cn}^\dagger(t-s_1) \\
&\qquad \times e^{-i(\omega_c-\omega_N)s_1}e^{i(\phi_N-\phi_B)}
\end{aligned} \tag{S9}$$

where ω_c is the frequency of core state c at time t. $\boldsymbol{\mathcal{E}}_N$ is the narrowband probe pulse and $\mathcal{E}_N$

its pulse envelope. We have assumed $\boldsymbol{\mathcal{E}}_N(t) = \mathcal{E}_N(t)e^{-i\omega_N t}e^{i\phi_N}$. ω_N is the center frequency of the narrowband probe $\boldsymbol{\mathcal{E}}_N$. $\mathcal{E}_B(\omega)$ is the broadband probe field envelope in frequency domain. The transition dipole matrix elements μ_{ij} are the components along the incoming field polarizations.

We shall factorize out the electronic modulation: $c_n(t) = \tilde{c}_n(t)e^{-i\omega_n t}$. The signal can then be rewritten as

$$S(\omega, \omega_N, T) = \Re\mathcal{E}_B^*(\omega) \sum_{nmc} \int_{-\infty}^{\infty} dt \int_0^{\infty} ds_1 e^{i(\omega-\omega_N-\omega_{nm})(t-T)}$$
$$\times \mathcal{E}_N(t-s_1-T)\tilde{c}_n(t-s_1)\tilde{c}_m^*(t)\mu_{mc}(t)\mu_{cn}^\dagger(t-s_1)e^{-i(\omega_{cn}-\omega_N)s_1}e^{i(\phi_N-\phi_B)}, \quad \text{(S10)}$$

in which the two resonance conditions to give a finite signal are clearly shown: first, $\omega_N = \omega_{cn}$ and second, $\omega = \omega_N + \omega_{nm}$.

Computational Details for the Surface Hopping Nonadiabatic Dynamics

The surface hopping simulation protocol implemented in SHARC[3,4] program was employed to simulate the nonadiabatic photodissociation of thiophenol. Details of the protocol are given in ref.[4]. The electronic structure calculations were performed using MOLPRO[5] program at the state-averaged CASSCF(4/6)/6-31G* level of theory with four lowest adiabatic electronic states are taken into account. The local diabatization algorithm based on the overlap matrices between the adiabatic electronic states $\langle\psi_\beta(t)|\psi_\alpha(t+\Delta t)\rangle$ is used to propagate the electronic wavefunction under the effect of nonadiabatic couplings, while the nuclear coordinates are propagated using Newton's equations. Surface hopping probability is calculated as described in ref.[4]. Given the coefficient vectors $\boldsymbol{c}(t)$ and $\boldsymbol{c}(t+\Delta t)$ and the corresponding

propagator matrix $\boldsymbol{P}$, hopping probabilities from electronic state β to α is calculated by

$$h_{\beta\to\alpha} = \left(1 - \frac{|c_\beta(t+\Delta t)|^2}{|c_\beta(t)|^2}\right) \frac{\Re\left[c_\alpha(t+\Delta t)(P_{\alpha\beta})^*(c_\beta(t))^*\right]}{|c_\beta(t)|^2 - \Re\left[c_\beta(t+\Delta t)(P_{\beta\beta})^*(c_\beta(t))^*\right]}. \tag{S11}$$

We employed the energy-based decoherence correction scheme to describe the electronic decoherence,[6] in which the wavefunction coefficients are rescaled according to the relation below.

$$c'_\alpha = c_\alpha \cdot \exp\left[-\Delta t \frac{|E_\alpha - E_\beta|}{\hbar}\left(1 + \frac{C}{E_{\text{kin}}}\right)^{-1}\right], (\alpha \neq \beta), \tag{S12}$$

$$c'_\beta = \frac{c_\beta}{|c_\beta|} \cdot \left[1 - \sum_{\alpha\neq\beta} |c'_\alpha|^2\right] \tag{S13}$$

The electronic population (ρ_{ii}; diagonal element of the density matrix) and the coherence (ρ_{ij}; off-diagonal element of the density matrix) in the adiabatic electronic state can be calculated from the wavefunction coefficient vector $\boldsymbol{c}(t)$, $\rho_{ii}(t) = |c_i(t)|^2$ and $\rho_{ij}(t) = c_i(t)c_j^*(t)$. The energy difference $|\Delta E_{ij}| = |E_j - E_i|$ was obtained from the energy difference between the adiabatic electronic states S_i and S_j. All quantities presented in the paper are in the adiabatic electronic basis. The total propagation time was 49 fs and the time steps for propagation of the nuclear and the electronic degrees of freedom were 0.05 fs and 0.002 fs, respectively. We sampled 45 initial geometries by using the quantum harmonic oscillator Wigner distribution around the ground state equilibrium geometry. The nonadiabatic surface hopping dynamics was initiated by promoting the system on S_2 ($^1\pi\sigma^*$) state. 45 trajectories were simulated and averaged out to provide the signals. Figures S3-S10 show the convergence of the population dynamics ρ_{ii} and coherences ρ_{12} and ρ_{01} with the number of trajectories taken into account.

We have investigated the dynamics of the S-H dissociation of thiophenol that takes place after its initial photoexcitation in S_2 ($^1\pi\sigma^*$) state (impulsive excitation approximation; no external pump pulse was taken into account in the surface hopping dynamics). In practice,

excitation at long wavelength $\lambda > 275\,\mathrm{nm}$ excites the system to $1^1\pi\pi^*$ state, while the $^1\pi\sigma^*$ state can be excited at shorter excitation wavelengths.[7–9] H-tunnelling from $1^1\pi\pi^*$ state to $^1\pi\sigma^*$ state may play a role in the photodissociation of thiophenol after an excitation to S_1 ($1^1\pi\pi^*$) state, which may not be properly described by the semi-classical surface hopping method. It is known that H-tunnelling plays an important role in a photodissociation of phenol after excitation to S_1 ($1^1\pi\pi^*$) state.[10–12] Therefore, a photodissociation dynamics following an initial excitation to S_2 ($^1\pi\sigma^*$) state was considered in this paper.

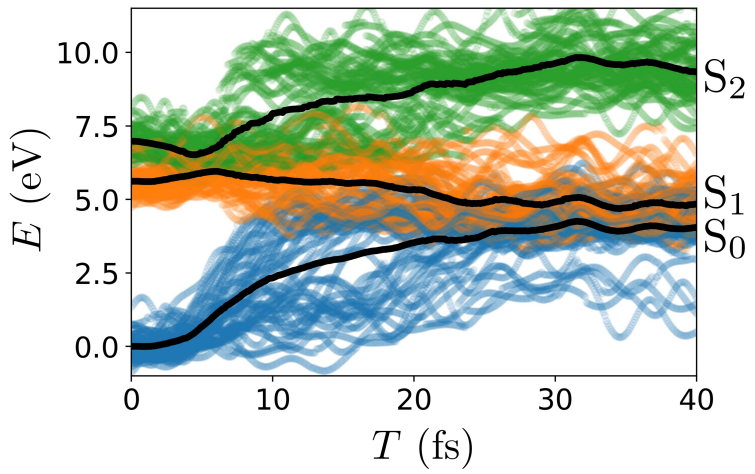

Figure S2: Adiabatic electronic energies of the valence electronic states of all trajectories (Blue: S_0, orange: S_1, and green: S_2) and their averages (black solid lines).

References

(1) Mukamel, S.; Rahav, S. *Advances In Atomic, Molecular, and Optical Physics*; Elsevier, 2010; Vol. 59; pp 223–263.

(2) Kowalewski, M.; Fingerhut, B. P.; Dorfman, K. E.; ; Bennett, K.; Mukamel, S. Simulating Coherent Multidimensional Spectroscopy of Nonadibatic Molecular Processes: From the Infrared to the X-Ray Regime. *Chem. Rev.* **2017**, in press.

(3) Mai, S.; Marquetand, P.; González, L. A general method to describe intersystem

crossing dynamics in trajectory surface hopping. *Int. J. Quantum Chem.* **2015**, *115*, 1215–1231.

(4) Richter, M.; Marquetand, P.; González-Vázquez, J.; Sola, I.; González, L. SHARC: ab initio Molecular Dynamics with Surface Hopping in the Adiabatic Representation Including Arbitrary Couplings. *J. Chem. Theory Comput.* **2011**, *7*, 1253–1258.

(5) Werner, H.-J.; Knowles, P. J.; Knizia, G.; Manby, F. R.; Schütz, M. Molpro: a general-purpose quantum chemistry program package. *WIREs Comput Mol Sci* **2012**, *2*, 242–253.

(6) Granucci, G.; Persico, M.; Zoccante, A. Including quantum decoherence in surface hopping. *J. Chem. Phys.* **2010**, *133*, 134111.

(7) Lim, J. S.; Choi, H.; Lim, I. S.; Park, S. B.; Lee, Y. S.; Kim, S. K. Photodissociation Dynamics of Thiophenol-d_1 : The Nature of Excited Electronic States along the S-D Bond Dissociation Coordinate. *J. Phys. Chem. A* **2009**, *113*, 10410–10416.

(8) Devine, A. L.; Nix, M. G. D.; Dixon, R. N.; Ashfold, M. N. R. Near-Ultraviolet Photodissociation of Thiophenol. *J. Phys. Chem. A* **2008**, *112*, 9563–9574.

(9) Venkatesan, T. S.; Ramesh, S. G.; Lan, Z.; Domcke, W. Theoretical analysis of photoinduced H-atom elimination in thiophenol. *J. Chem. Phys.* **2012**, *136*, 174312.

(10) Yang, K. R.; Xu, X.; Zheng, J.; Truhlar, D. G. Full-dimensional potentials and state couplings and multidimensional tunneling calculations for the photodissociation of phenol. *Chem. Sci.* **2014**, *5*, 4661–4680.

(11) Xu, X.; Zheng, J.; Yang, K. R.; Truhlar, D. G. Photodissociation Dynamics of Phenol: Multistate Trajectory Simulations including Tunneling. *J. Am. Chem. Soc.* **2014**, *136*, 16378–16386.

(12) Xie, C.; Ma, J.; Zhu, X.; Yarkony, D. R.; Xie, D.; Guo, H. Nonadiabatic Tunneling in Photodissociation of Phenol. *J. Am. Chem. Soc.* **2016**, *138*, 7828–7831.

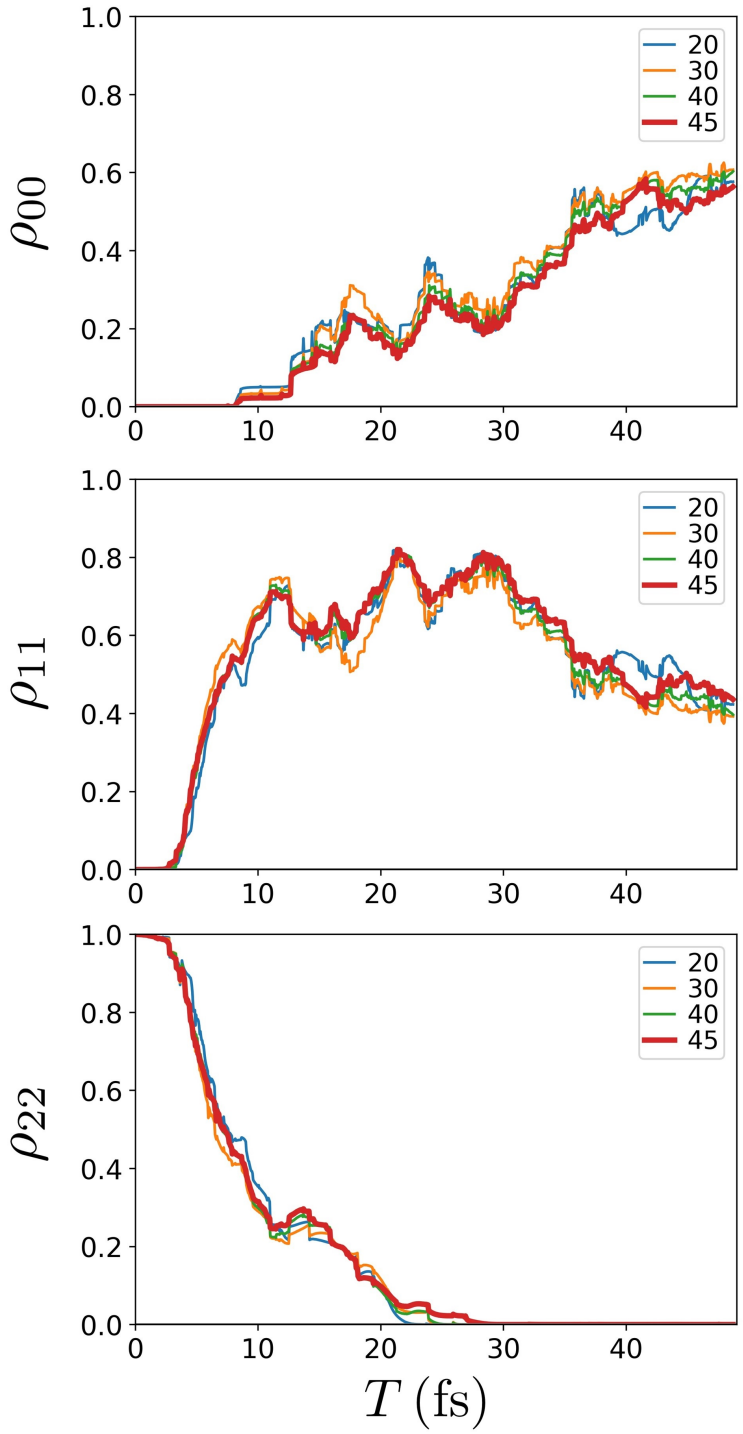

Figure S3: Convergence of the population dynamics ρ_{ii} for S_i state with the number of trajectories.

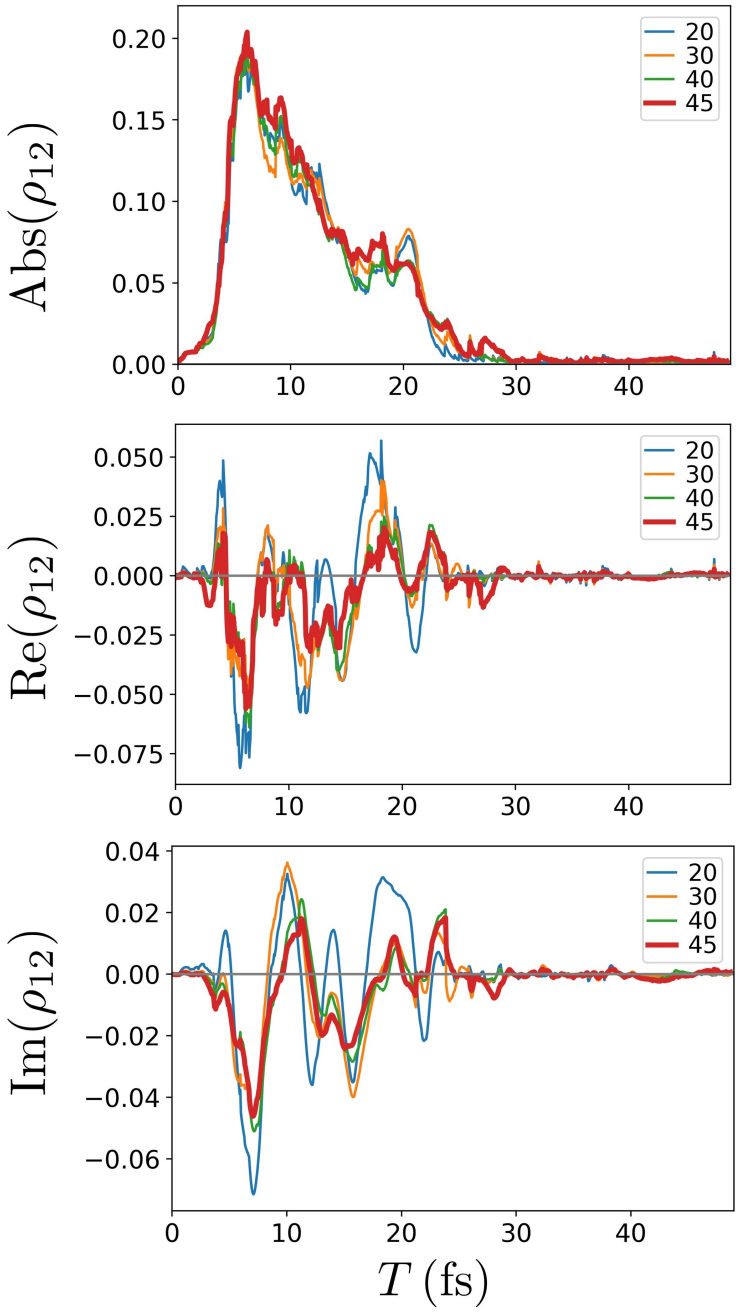

Figure S4: Convergence of the absolute, real, and imaginary values of the coherence $\rho_{12}(T)$ with the number of trajectories.

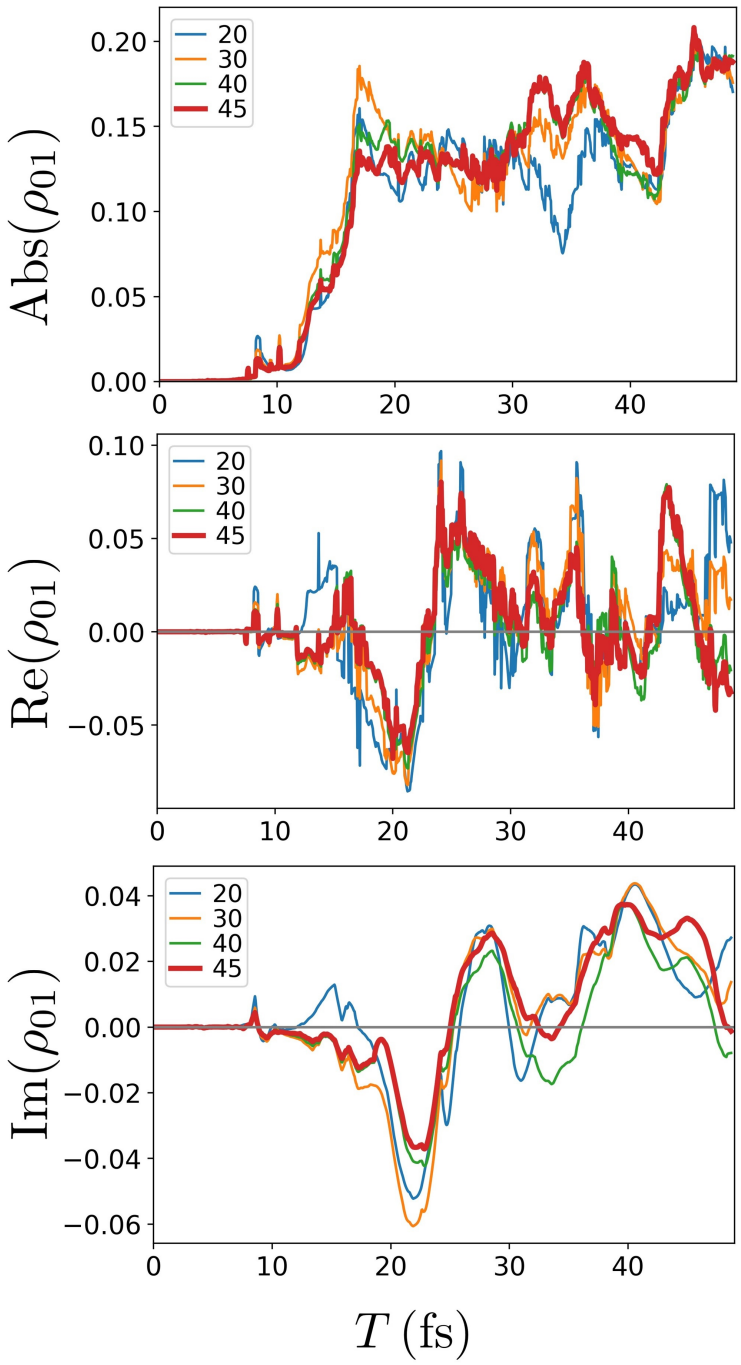

Figure S5: Convergence of the absolute, real, and imaginary values of the coherence $\rho_{01}(T)$ with the number of trajectories.

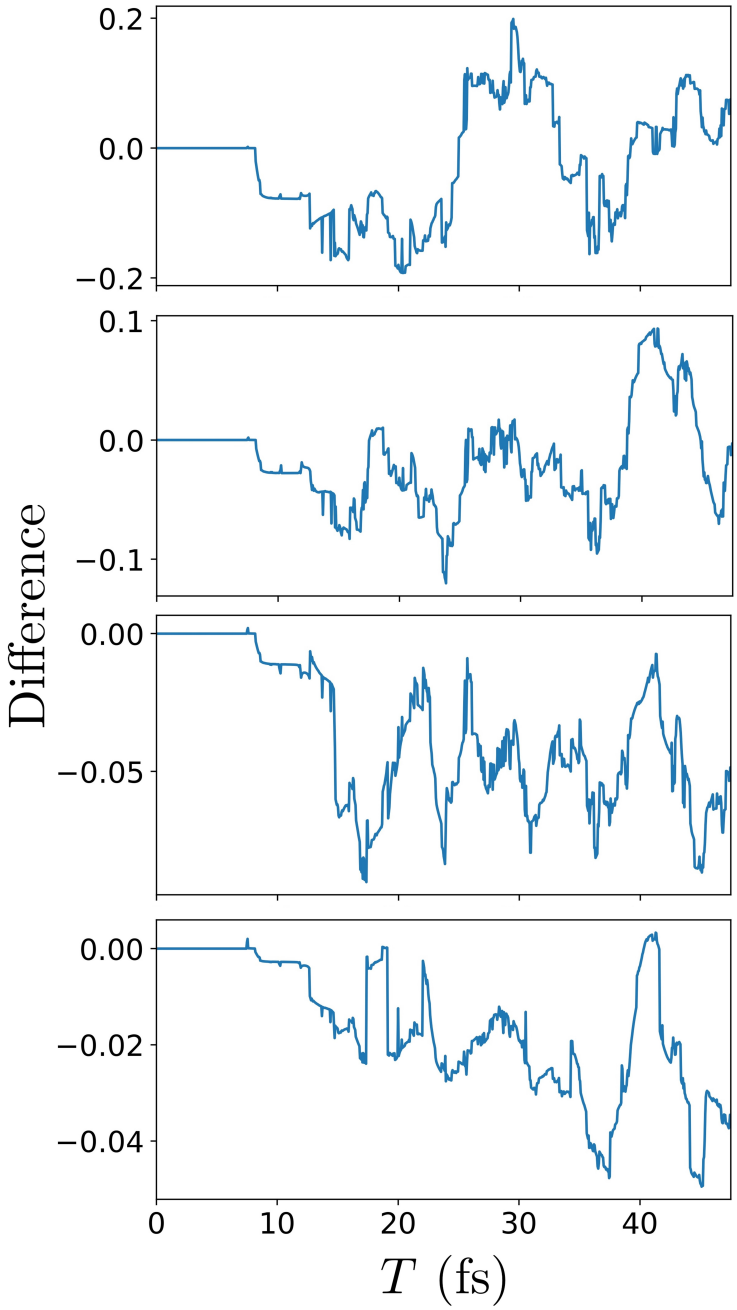

Figure S6: Difference between the population ρ_{00} averaged over all trajectories and several number of trajectories. Number of trajectories are 10, 20, 30, and 40 from the top.

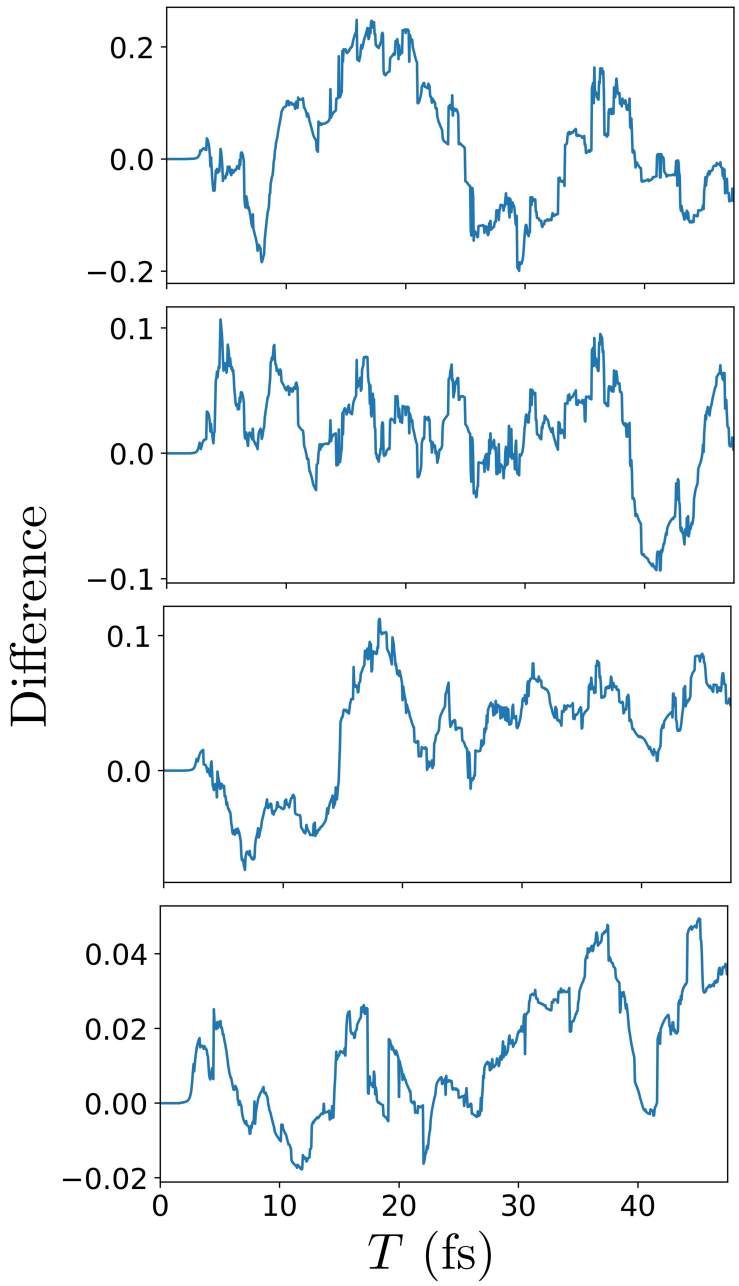

Figure S7: Same as Figure S6 but for the population ρ_{11}.

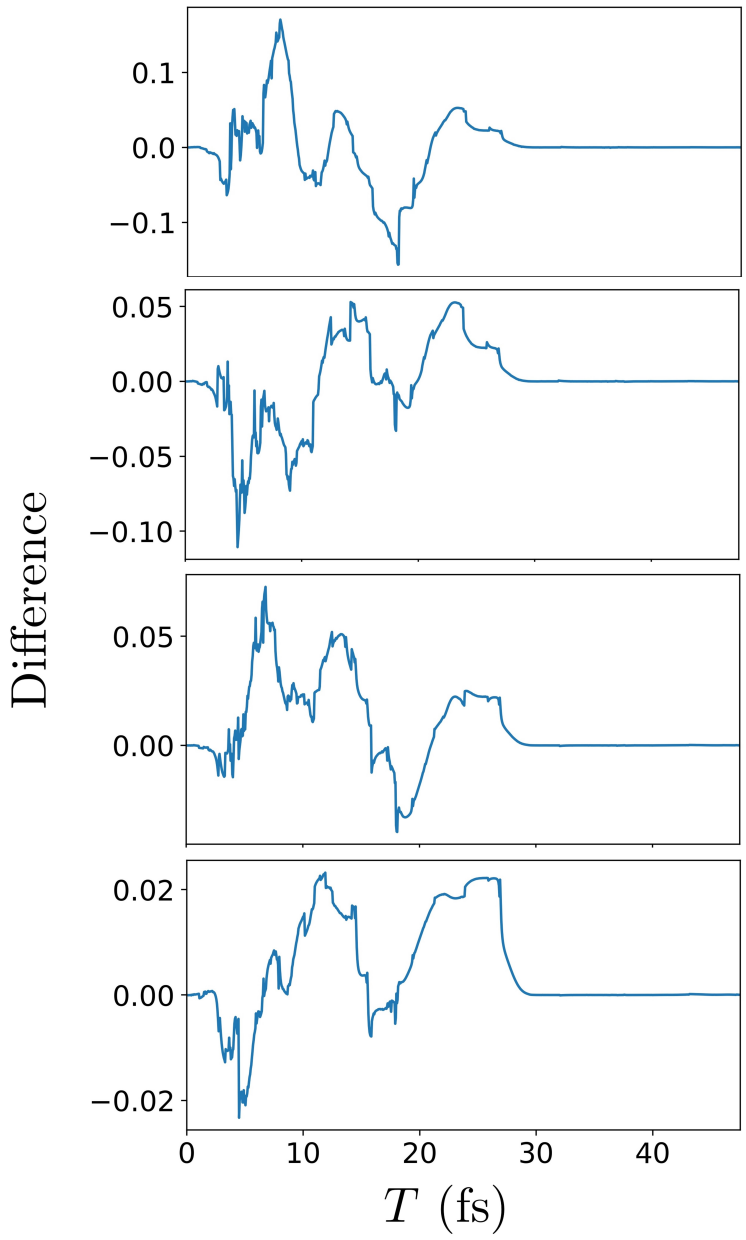

Figure S8: Same as Figure S6 but for the population ρ_{22}.

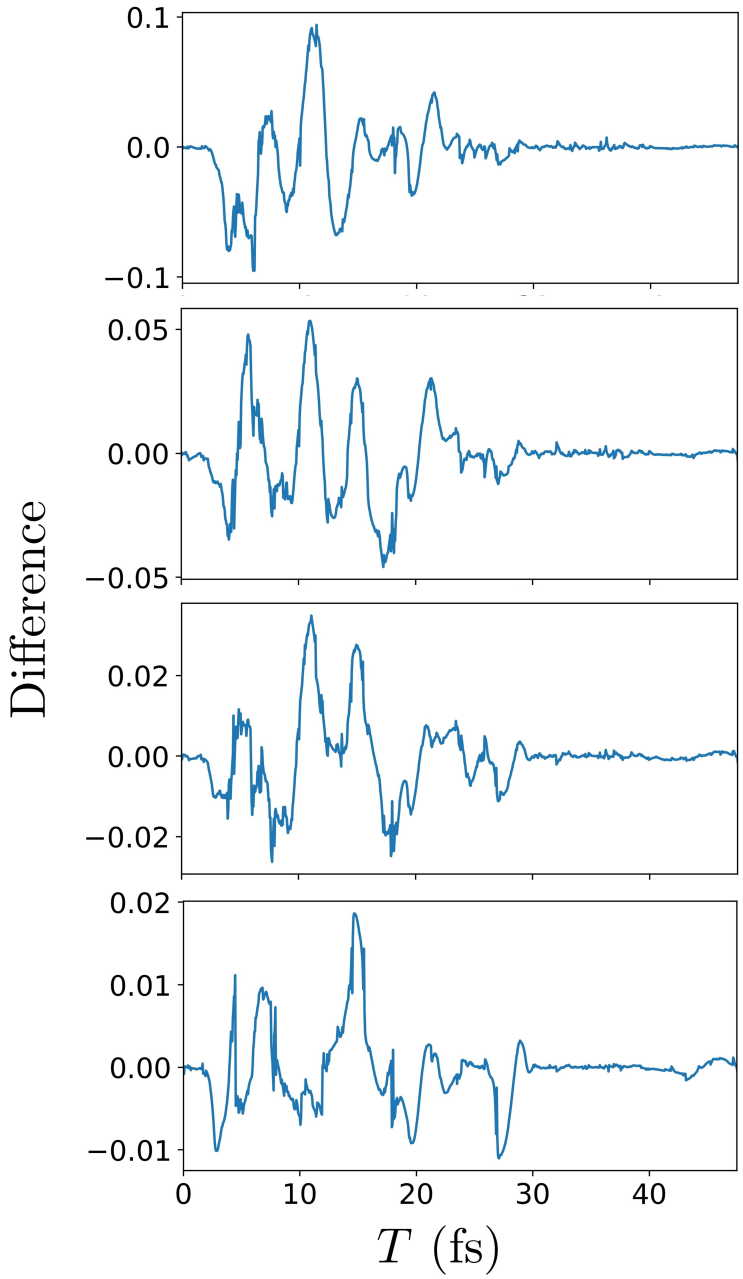

Figure S9: Same as Figure S6 but for the real part of the coherence $\mathrm{Re}(\rho_{12})$.

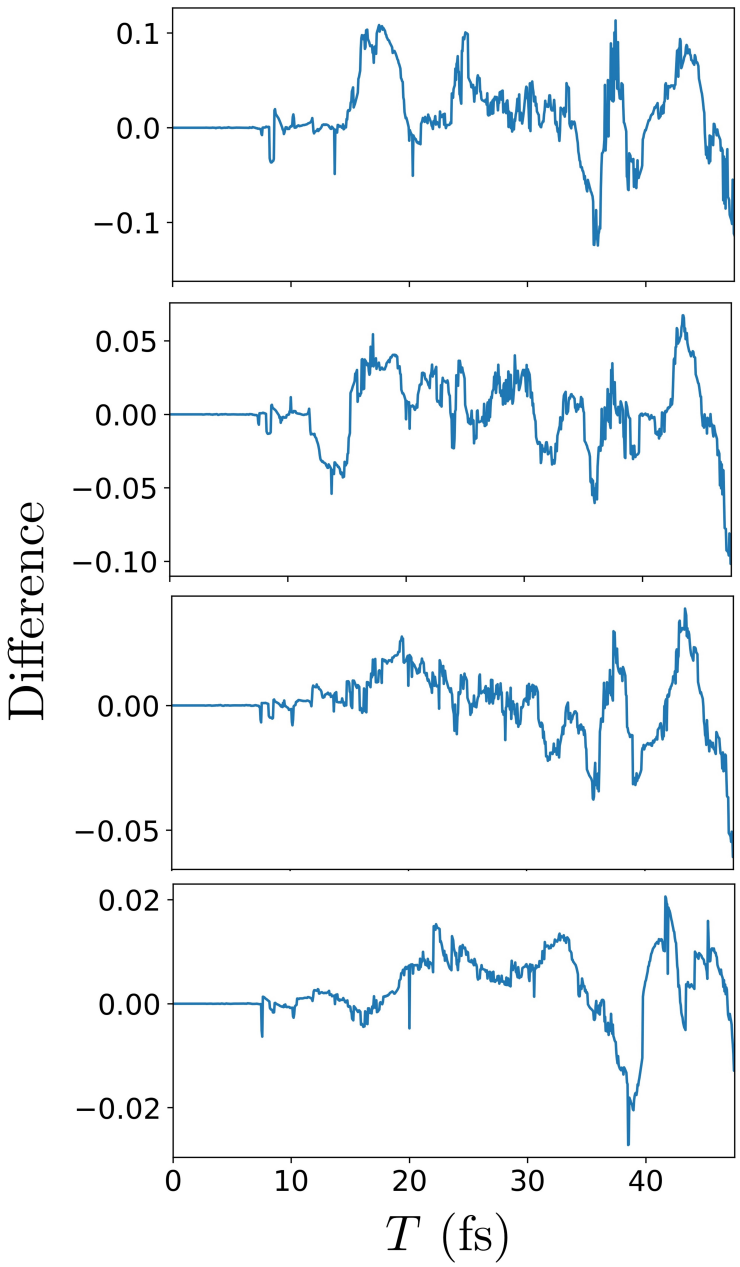

Figure S10: Same as Figure S6 but for the real part of the coherence $\mathrm{Re}(\rho_{01})$.